

Research article

Ammonia chemistry and oxidation dynamics as dual driving factors of PM_{2.5} nitrate pollution: Insights from the spatiotemporal disparities in central China



Shuangliang Ma ^{a,b,*} , Nan Wang ^{b,c}, Jiani Zhang ^{a,d}, Daiqi Ye ^{a,d,**}, Lingling Wang ^b

^a School of Environment and Energy, South China University of Technology, Guangzhou, 510006, China

^b Henan Ecological Environment Monitoring and Safety Center, Henan Key Laboratory of Environmental Monitoring Technology, Zhengzhou, 450001, China

^c College of Global Change and Earth System Science, Faculty of Geographical Science, Beijing Normal University, Beijing, 100875, China

^d National Engineering Laboratory for Volatile Organic Compounds Pollution Control Technology and Equipment, Guangzhou, 510006, China

A B S T R A C T

Despite marked improvements in air quality across China, nitrate-driven PM_{2.5} pollution in central China has exhibited divergent trends tied to urbanization gradients, with underlying mechanisms remaining poorly understood. Through six cold-season observational campaigns (2017/2018–2022/2023) across urban, rural, and suburban sites, we identified ammonia-dominated chemistry and oxidation dynamics as dual drivers of contrasting nitrate trends. Despite substantial NO₂ reductions (~34.7 %), urban nitrate increased by 20.4 %, driven by lack of coordinated NH₃ control (+16.1 %) and enhanced oxidation. The intensity of heterogeneous reactions increased the most during observations due to elevated aerosol water content and particle acidity. In contrast, rural and suburban regions achieved nitrate declines (12.4 % and 9.0 %, respectively) through synchronized NH₃–NO₂ co-reductions, which countered oxidation enhancement despite higher NH₃. De-weathered nitrate still rose 2.8 % at the urban site but decreased by 20.1 % and 23.3 % at rural and suburban sites, further confirming urban NO_x-only strategies fail to curb nitrate pollution due to ammonia buffering and enhanced oxidation. To address this, we propose a region-specific framework: 1) prioritizing agricultural NH₃ mitigation in rural zones, 2) targeting non-agricultural NH₃ and oxidant precursors in urban hotspots, and 3) implementing hybrid emission trading systems in transitional suburbs. This study provides actionable insights for managing multi-pollutant synergies in rapidly urbanizing regions where agricultural and industrial activities intersect.

1. Introduction

Over the past decade, significant reductions in PM_{2.5} concentrations have been observed in key regions like the Beijing-Tianjin-Hebei area and the Yangtze River Delta, due to comprehensive clean air initiatives by the Chinese government (Geng et al., 2024). However, The China High Air Pollutants dataset (<https://weijing-rs.github.io/product.html>) further shows that severe PM_{2.5} pollution has shifted from the Beijing-Tianjin-Hebei region to north-central Henan in recent years. Henan Province, which is located in the central part of China, emerged as the region with the highest PM_{2.5} concentrations from the start of the 14th Five-Year Plan (<https://english.mee.gov.cn/Resources/Reports/soe/>). Among the primary water-soluble inorganic components of PM_{2.5}, sulfate (SO₄²⁻) has decreased significantly, while NO₃⁻ and ammonium (NH₄⁺) levels have remained relatively stable (Lei et al., 2021; Zhai et al., 2021; M. Zhou et al., 2022a). High nitrate concentrations in the atmosphere pose serious health risks and contribute to

excessive nitrogen deposition, which adversely affects aquatic ecosystems (Feng et al., 2024; Liu et al., 2013; Tian et al., 2024). Nitrate formation in the troposphere mainly occurs through the oxidation of nitrogen dioxide (NO₂) via a series of atmospheric reactions (Brown et al., 2004; Chen et al., 2020). Daytime oxidation of NO₂ to nitric acid (HNO₃) by hydroxyl radicals (OH) is predominant, while at night, the heterogeneous uptake of dinitrogen pentoxide (N₂O₅) is the main pathway. Nitrates then partition into the particle phase, influenced by factors such as ammonia (NH₃) availability, temperature, and relative humidity (Guo et al., 2018; Wang et al., 2018). Previous studies have suggested that nonlinear photochemical and aerosol feedback mechanisms attenuate the response of nitrate to reductions in anthropogenic NO_x emissions. For instance, Fu et al. (2020) reported a 31.8 % reduction in NO_x emissions in North China from 2011 to 2017, but nitrate levels showed minimal change, largely due to a 30 % increase in ozone (O₃) and hydroxyl radical (OH) concentrations. Zhou et al. (M. Zhou et al., 2022a) attributed subtle nitrate variations in Shanghai from 2011

* Corresponding author. School of Environment and Energy, South China University of Technology, Guangzhou, 510006, China.

** Corresponding author. School of Environment and Energy, South China University of Technology, Guangzhou, 510006, China.

E-mail addresses: esleeloomsl@mail.scut.edu.cn (S. Ma), cedqye@scut.edu.cn (D. Ye).

to 2019 to enhanced hydrolysis of N_2O_5 , while Lei et al. (2021) linked the increasing nitrate contribution to air pollution in Beijing's cold season from 2013 to 2020 to enhanced ozone and nitrogen oxidation efficiencies. Climate, geographical location, and emission levels create distinct aerosol composition changes across different regions of China. However, research on long-term temporal and spatial variations in aerosol composition in central China remains limited.

Most studies on central China have focused on short-term pollution events and meteorological factors. Wang et al. (2022) found that secondary aerosol formation in Henan province, situated within Central Plains of China, was closely linked to high NH_3 emissions primarily driven by intensive agricultural activities characteristic of this historical breadbasket region. As the primary alkaline component in the atmosphere, NH_3 influences aerosol chemistry, and the formation of ammonium nitrate (NH_4NO_3) is not limited by NH_3 availability in ammonia-rich environments (Guo et al., 2018). Du et al. (2020) and Yang et al. (2021) highlighted that prolonged heavy pollution episodes in central China were closely tied to the unique climate and geographical features, which contribute to a pollution delay effect and elevated transport rates compared to neighboring provinces. Secondary $\text{PM}_{2.5}$ transport within a 200-km radius can account for 60 %–80 % of pollution. While primary emissions in Henan were lower than those in surrounding industrial provinces from the Multi-resolution Emission Inventory model (<http://meicmodel.org/>), concentrations of secondary water-soluble inorganic ions (SWI) especially NO_3^- have already exceeded those in Hebei and Shandong (Liu et al., 2022). Despite recent progress, the key mechanisms underlying nitrate variability in central

China remain a critical research gap.

Changes in aerosol composition are influenced by both meteorological conditions and emission levels. A comparative analysis of modeling methods by Zheng et al. (2023) and Vu et al. (2019) suggest that machine learning techniques can effectively address this complexity. Integrating observational data with model simulations is crucial to understanding the long-term effects of meteorological and emission factors on aerosol chemistry.

Our study establishes an integrated observational and modeling framework to investigate nitrate dynamics and their drivers across urban–suburban–rural gradients in ammonia-abundant central China. Through six consecutive cold-season campaigns (2017/2018–2022/2023), we aim to: (1) characterize long-term spatiotemporal variations in aerosol composition, emphasizing divergent trends linked to urbanization gradients; (2) quantify responses of nitrate-dominated aerosols to gaseous precursors (e.g., NO_2 , NH_3) and meteorological factors; and (3) unravel the synergistic mechanisms between ammonia-rich aerosol chemistry and oxidants in shaping nitrate formation pathways. This study advanced a novel approach to track aerosol responses to emission controls and provides actionable insights for region-specific nitrate mitigation strategies, addressing the unique challenges of integrated agricultural-industrial zones.

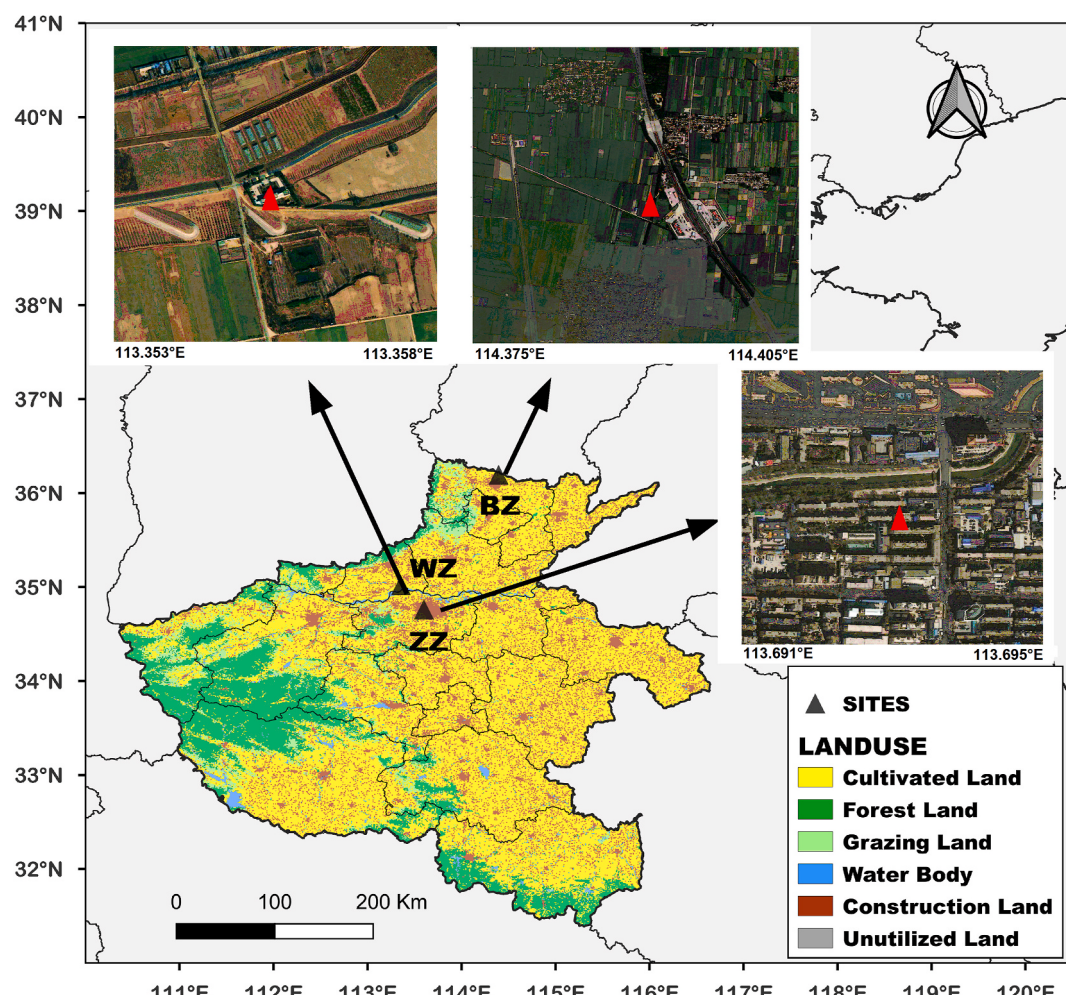


Fig. 1. Locations and the surrounding environment of the sampling sites (ZZ-urban, WZ-rural, and BZ-suburban).

2. Materials and methods

2.1. Sampling sites and chemical analysis

The urban site is located on the roof of the Henan Ecological Environmental Monitoring and Safety Center (ZZ, 34.86°N, 113.6°E) in the heart of Zhengzhou (Fig. 1), the capital of Henan Province. Surrounded by major traffic routes and residential areas, this site is part of one of the "2 + 36" key cities targeted for air quality research in China. The suburban site is situated in Beijie Village (BZ, 36.19°N, 114.39°E), Baizhuang Town, Anyang City, near the border between Henan and Hebei provinces. It is located close to major highways, including the Beijing-Hong Kong-Macao Expressway and Anyang Ring Highway, and lies within the southern part of the Beijing-Tianjin-Hebei transmission channel. The rural site is located on the roof of the Yellow River Bureau in Jefeng Village, Wuzhi County (WZ, 35.02°N, 113.36°E), about 20 km from the urban center of Jiaozuo. Surrounded by farmland and livestock areas, this site is free from industrial emissions and vehicle pollution. It is situated near the Yellow River, approximately 2.3 km from its banks. The strategic placement of these sites captures representative pollution profiles along an urbanization gradient: ZZ represented intense anthropogenic emissions in a megacity core, WZ reflected agricultural-dominated rural environments, and BZ characterized vehicle-dominated suburban areas influenced by regional transport. The WZ and BZ sites are located 50 km and 150 km away from ZZ respectively, effectively avoiding non-point source pollution influences from the megacity core. All three stations reside within a unified geographic region, exhibiting consistent annual pollution seasonality patterns (Fig. S1). During winter periods, the sites share coherent meteorological systems with synchronized fluctuations in humidity, atmospheric pressure, and precipitation (Fig. S1), thereby ensuring that observed inter-station differences predominantly derive from emission regime variations rather than meteorological disparities. The sampling campaign was conducted during the cold seasons in the years 2017/2018, 2018/2019, 2019/2020, 2020/2021, 2021/2022, and 2022/2023 (e.g. November and December 2017, as well as January and February 2018, represented the cold season of 2017/2018).

The online monitors for aerosols and gases in ambient air (MARGA2080, Metrohm, Switzerland) were used to measure water-soluble inorganic ions (SWI, including NH_4^+ , Na^+ , Mg^{2+} , K^+ , Ca^{2+} , NO_3^- , SO_4^{2-} , Cl^-) in $\text{PM}_{2.5}$ and trace gases (NH_3 , HONO , HNO_3) at hourly intervals. Semi-continuous carbon analyzers (Model-4, Sunset Laboratory, USA) were used to measure elemental carbon (EC) and organic carbon (OC). Concentrations of NO_2 , SO_2 , and O_3 were measured using the following instruments: NO- NO_2 -NOx analyzers (42i, Thermo Fisher), SO_2 analyzers (43i, Thermo Fisher), and O_3 analyzers (49i, Thermo Fisher). The mass concentration of $\text{PM}_{2.5}$ was measured with Thermo Fisher 5030i. Detailed quality assurance and quality control (QA/QC) procedures for these instruments are provided in the supplementary materials (Text S1). Meteorological data, including temperature (Temp), wind speed (WS), wind direction (WD), pressure (Press), precipitation, and relative humidity (RH), were recorded every 5 min.

2.2. Prediction of aerosol water content and pH

The thermodynamic model ISORROPIA-II was used to estimate aerosol pH and aerosol water content ($\text{AWC} \approx \text{AWC}_i$, aerosol water content of inorganic species) (Fountoukis and Nenes, 2007). The aerosol pH and AWC were calculated based on the concentrations of K^+ , Ca^{2+} , Mg^{2+} , TNH_X (gas NH_3 plus NH_4^+), total sulfate concentration (TH_2SO_4 , replaced by SO_4^{2-}), total sodium (TNa , replaced by Na^+), TCI (HCl trace and high uncertainty, Cl^- instead) and TNO_3 (HNO_3 trace, instead of NO_3^-) and meteorological parameters (RH, temperature). We used the "forward" mode of ISORROPIA-II, as it is less sensitive to errors than the "reverse" mode (Ding et al., 2019; Guo et al., 2015; Song et al., 2018). Aerosol pH was calculated using the formula from Guo et al. (2015). In

addition, we refer to previous studies and exclude pH data with RH < 30 %, where the correlation between predicted and observed values of nitrate partition between gas and particulate phases is weak. Furthermore, we exclude AWC data with RH > 95 % and there was precipitation due to the potential uncertainty in AWC estimation caused by small deviations in measured relative humidity.

2.3. Machine learning model

A machine learning model using a random forest algorithm was applied to assess the impact of emissions and meteorological factors on pollutant concentrations. This method, first introduced by Grange et al. (2018) and enhanced with the "rmweather" R package (Vu et al., 2019), uses time variables (data_unix, data_julian, hour, week, day) and meteorological parameters (temperature, relative humidity, wind speed, wind directs, precipitation, pressure) as input features. Building on the refined methodology for discontinuous time-period comparisons developed by Shi et al. (2021) and Zhang et al. (2020), we implemented these enhancements in our simulation. The model's de-weathered NO_3^- concentration reflects the influence of emissions alone. Separate models were created for each of the three sampling sites. We set the number of trees to 300 ($n_{\text{trees}} = 300$) and randomly sampled 300 observations ($n_{\text{samples}} = 300$) for each training iteration. Node splitting rules used the "extratrees" method, which enhances generalizability through randomized feature split points. Model optimization utilizes Monte Carlo cross-validation with 1000 iterations, each employing a randomized 70 % training and 30 % testing partition. Feature selection at each node was randomized from all predictors except the explicitly included temporal variables. Performance metrics include RMSE, R^2 values, and residual distributions were shown in Table S5 and Fig S14–16. Variable importance was quantified via permutation importance. These values align closely with previous similar reports (W. Zhou et al., 2022; Zhang et al., 2020).

3. Results

3.1. Long-term trends of $\text{PM}_{2.5}$ nitrate and other species

Over the six cold seasons, $\text{PM}_{2.5}$ concentrations decreased at the ZZ, WZ, and BZ sites by 18.2 %, 10.8 %, and 26.3 %, respectively, reflecting a significant reduction in high concentrations and an overall improvement in air quality from the Three-year Action Plan (2018–2020) (Fig. 2, Tables S1, S2, and S3). The peak $\text{PM}_{2.5}$ concentration occurred during the 2018/2019 cold season, mainly due to unfavorable meteorological conditions (as detailed in Section 3.4), while the most significant decline was observed in the 2021/2022 cold season, influenced by the COVID-19 pandemic and regional measures for the Winter Olympics (Nie et al., 2021; Qu et al., 2024; Ryoo et al., 2024; Zhai et al., 2021). However, the concentrations at the three sites consistently remained within a relatively high range of $64.5 \pm 42.5 \mu\text{g m}^{-3}$ to $142.8 \pm 87.5 \mu\text{g m}^{-3}$, marked by exceeding the warm-season average (~below $30 \mu\text{g m}^{-3}$, Fig. S1). Although severe pollution episodes were largely mitigated during the warm season, such events continued to occur frequently during winter. Air quality was categorized into three levels based on hourly $\text{PM}_{2.5}$ concentrations: clean (C) with $\text{PM}_{2.5} \leq 75 \mu\text{g m}^{-3}$, moderate pollution (MP) with $\text{PM}_{2.5}$ between 75 and $150 \mu\text{g m}^{-3}$, and heavy pollution (HP) with $\text{PM}_{2.5} > 150 \mu\text{g m}^{-3}$. Fig. 2 illustrates the proportion of air pollution levels across the six cold seasons at the three sites. The MP and HP periods were generally highest at BZ, followed by WZ and ZZ, indicating poorer air quality in suburban and rural areas compared to the urban. Over time, the proportion of HP periods decreased at all sites, particularly at BZ, where it dropped from 29 % to 10.7 %, at ZZ, where it fell from 14.6 % to 9.2 %, and at WZ, where it fell from 19.5 % to 13.6 %. These trends highlight the effectiveness of clean air measures in reducing severe haze events and PM load, although air quality improvements in rural areas were still limited. Low temperature and high

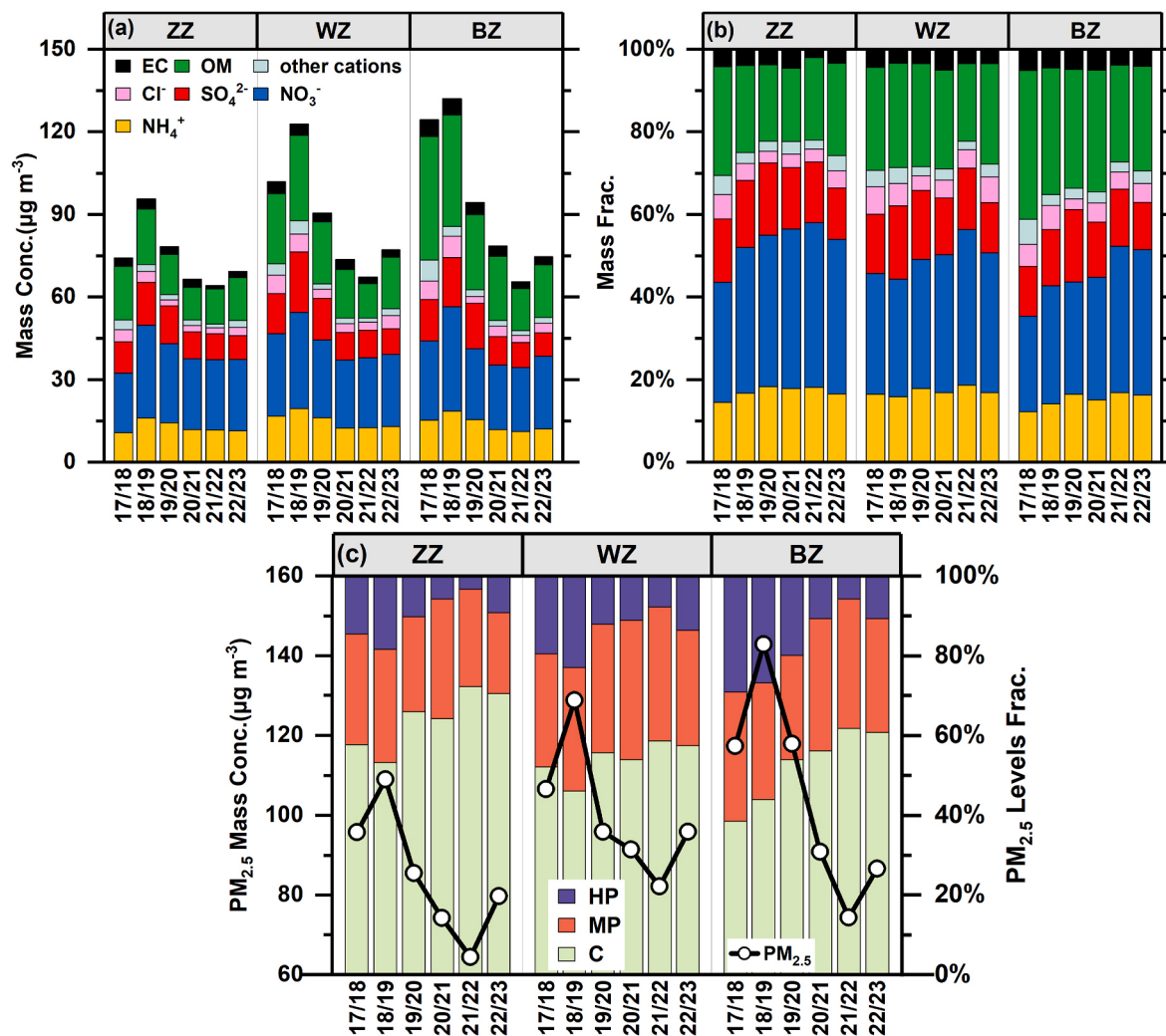


Fig. 2. (a, b) Changes of mass concentrations and mass fractions of PM_{2.5} species at the ZZ, WZ, and BZ sites in cold seasons from 2017/2018 to 2022/2023. (c) Changes of mass concentrations and levels fractions of PM_{2.5} at the ZZ, WZ, and BZ sites during cold seasons from 2017/2018 to 2022/2023. Three p.m._{2.5}-based categories: C (Clean: $\leq 75 \mu\text{g m}^{-3}$), MP (Moderate Pollution: $75\text{--}150 \mu\text{g m}^{-3}$), HP (Heavy Pollution: $>150 \mu\text{g m}^{-3}$).

humidity conditions during cold seasons promote the heterogeneous conversion of gaseous precursors (NO₂, NH₃) to particulate NO₃⁻, while enhancing the synergistic effects of aerosol properties (Zheng et al., 2020; M. Zhou et al., 2022b). Thus, research on reducing PM_{2.5} and its chemical components during cold seasons holds critical implications for pollution mitigation in central China.

The mass concentrations of SO₄²⁻, organic matters (OM = OC × 1.6) (Turpin and Lim, 2001), and NO₃⁻ were the main contributors to PM_{2.5} at all sites (Fig. 2, Tables S1, S2, and S3). The hourly concentrations of PM_{2.5} water-soluble inorganic cations and anions over the years exhibited a strong correlation, as showed in Fig. S2. At ZZ and WZ, NO₃⁻ was the dominant species, followed by OM. However, at BZ, NO₃⁻ surpassed OM as the primary component in the last two cold seasons. The reduction of SO₄²⁻ and OM accounted for most of the decrease in PM_{2.5}, with the most notable reductions at BZ, which is near industrial areas, showing decreases of 53 % and 62 %, respectively. These reductions were likely driven by policies such as replacing coal with cleaner fuels and enforcing stringent control measures in the Beijing-Tianjin-Hebei region. However, NO₃⁻ and NH₄⁺ showed minimal reductions. In fact, NO₃⁻ at ZZ increased by 20.4 % from 21.6 $\mu\text{g m}^{-3}$ in 2017/2018 to 26.0 $\mu\text{g m}^{-3}$ in 2022/2023, and NH₄⁺ increased by 6.5 %. The WZ site dropped by 12.4 % and 22.6 % respectively, while the BZ site saw declines of 9.0 % and 19.7 % respectively. However, rebounds in NO₃⁻ and NH₄⁺ were observed at WZ and BZ in the last three cold seasons,

indicating a plateau in the reduction of these key species.

NO₃⁻ and NH₄⁺ were strongly correlated across all sites ($p < 0.001$ for hourly data, Fig. S2). At all three sites, the average concentration of NO₃⁻ remained above 23 $\mu\text{g m}^{-3}$, and NH₄⁺ concentrations were consistently above 11 $\mu\text{g m}^{-3}$. These concentrations observed were higher than those reported in other major Chinese cities, including Shanghai, Beijing, and Chengdu, as well as in rural areas of Sichuan and northwest China (Lei et al., 2021; Qi et al., 2024; N. Wang et al., 2023; M. Zhou et al., 2022a). The mass fraction of NO₃⁻ at ZZ increased from 29.0 % in 2017/2018 to 37.5 % in 2022/2023, it rose from 29.3 % to 33.4 % at WZ, and at BZ, it rose from 23.2 % to 35.1 %. The annual trend of NO₃⁻ as a percentage of PM_{2.5} increased consistently during the MP and HP periods, suggesting that nitrate has become a more dominant component in urban air pollution (Lei et al., 2021; M. Zhou et al., 2022a). Moreover, the mass fractions of NO₃⁻ in MP and HP levels has reached approximately 40 % over the last three cold seasons (Fig. S4). This trend was also reflected in the increasing NO₃⁻/SO₄²⁻ ratio, which reached 4.3–4.7 at the three sites in 2022/2023, compared to 2.5–2.9 in 2017/2018. In contrast, nitrate concentrations during the warm season exhibited a steady decrease, reaching an average of approximately 7 $\mu\text{g m}^{-3}$ in the 2022/2023 warm season (Fig. S1), with rare occurrences of high pollution episodes. This shift emphasizes the growing role of nitrate in PM_{2.5} and indicates that further reductions in PM_{2.5}, particularly during cold seasons, will face challenges (Geng et al., 2024).

3.2. Response of nitrate to NO_2 and related gaseous pollutants

The concentration of NO_2 , a precursor to NO_3^- , varied significantly across the sites (Fig. 3). During the first two cold seasons, NO_2 concentration was highest at ZZ, followed by BZ and WZ. However, in the following four seasons, BZ exhibited the highest NO_2 concentration. NO_2 showed the largest reduction at ZZ (34.7 %), a trend also observed in major cities like Beijing and Shanghai (Lei et al., 2021; M. Zhou et al., 2022a). WZ saw a decrease of 13.6 %, while BZ showed only a slight reduction of 1.4 %. The low reduction at BZ can be attributed to ongoing NO_x emissions from passing trucks, highlighting the importance of traffic control in urban and hub areas (Sun et al., 2020).

The nitrogen oxide ratio (NOR), defined as the molar ratio of $\text{NO}_3^- / (\text{NO}_3^- + \text{NO}_2)$, reflects the efficiency of nitrate formation from NO_2 . At ZZ, NO_3^- increased by $0.73 \mu\text{g m}^{-3} \text{yr}^{-1}$ (3.4 %), while NO_2 decreased by $3.28 \mu\text{g m}^{-3} \text{yr}^{-1}$ (5.78 %), resulting in NOR rising from 0.20 to 0.31 (Fig. 3 and S5). In contrast, BZ showed a linear decline in both NO_3^- ($0.43 \mu\text{g m}^{-3} \text{yr}^{-1}$) and NO_2 ($0.10 \mu\text{g m}^{-3} \text{yr}^{-1}$) (Fig. S7), with NOR decreasing from 0.31 to 0.26. WZ exhibited the highest NOR (0.28–0.35), with NO_3^- and NO_2 reductions of $0.62 \mu\text{g m}^{-3} \text{yr}^{-1}$ (2.06 %) and $0.87 \mu\text{g m}^{-3} \text{yr}^{-1}$ (2.26 %), respectively. The NOR values at WZ remained higher than at the other two sites, suggesting that NO_3^- formation in rural areas was more strongly influenced by factors other than precursor levels, such as atmospheric oxidizing capacity and aerosol acidity (Fig. S7). Fig. 3 demonstrates that all three sites exhibited a gradual increase in ozone concentrations over the years, which would enhance the $\text{NO}_2 + \text{O}_3 \rightarrow \text{NO}_3$ reaction pathway.

Ammonia, a key alkaline precursor of NH_4^+ , exhibited the highest concentrations at WZ (Table S2 and $19.1\text{--}28.4 \mu\text{g m}^{-3}$ each cold season), exceeding other rural areas in North China (Pan et al., 2018). ZZ had the lowest levels (Table S1 and $12.4\text{--}15.1 \mu\text{g m}^{-3}$), closely to Beijing and Tianjin during winter (Pan et al., 2018), indicating that ammonia emissions in rural areas were significantly more pronounced compared to urban and suburban areas. Over the study period, NH_3 concentrations declined by 7.3 % at BZ and 17.3 % at WZ, while increasing by 16.1 % at ZZ (Fig. 3 and S6). The observed spatial patterns combined with trend analyses reveal that rural decreases were mainly attributable to

agricultural emission reductions, while slightly growing winter NH_3 emissions from urban transport and industrial activities (surpassing agricultural contributions) partially counteracted agricultural mitigation effects (Zheng et al., 2024). Chamber experiments indicated that higher NH_3 concentrations can accelerate the conversion of NO_2 to NO_3^- (Behera, 2011), explaining the higher NOR observed at WZ. It is evident that the availability of NH_3 plays a key role in nitrate formation, as discussed in the next section in terms of aerosol chemistry related to NH_3 .

3.3. Changes in aerosol chemical properties and their impact on nitrates

The gas-particle distribution of aerosols, such as $\text{NH}_3/\text{NH}_4^+$ and $\text{HNO}_3/\text{NO}_3^-$, is influenced by chemical properties, particularly aerosol acidity and aerosol water content (AWC), which govern particle formation kinetics (Cheng et al., 2016; Zheng et al., 2020). Increased AWC promotes NH_4NO_3 formation, particularly enhancing the heterogeneous hydrolysis of N_2O_5 to form NO_3^- during the nighttime (Wang et al., 2018; M. Zhou et al., 2022b). The molar ratios of NO_3^- to $(\text{NO}_3^- + \text{HNO}_3)$ and NH_4^+ to $(\text{NH}_4^+ + \text{NH}_3)$, denoted as $\varepsilon(\text{NO}_3^-)$ and $\varepsilon(\text{NH}_4^+)$, respectively, reflect the gas-particle partitioning of these ions in the atmosphere. In this study, aerosol pH and AWC were obtained through a thermodynamic model. The simulated NH_3 showed a strong correlation with the observed NH_3 (Fig. S3, $R^2 = 0.93\text{--}0.99$), which proved the reliability of the results. Across all cold seasons at the three sites, AWC values, corresponding to RH, were subjected to nonlinear fitting. AWC exhibited exponential growth when RH exceeded 50 % (Table S4, Fig. S8) under MP and HP levels. Similar fluctuations were observed in AWC, NOR, and $\varepsilon(\text{NH}_4^+)$ under C, MP, and HP levels at 3 sites (Fig. 5). During HP periods, AWC values were approximately ten times greater than during C periods, accompanied by nearly a 100 % increase in NOR. The ZZ site showed the most pronounced increasing trend in AWC annually and exhibited a positive correlation with NOR during pollution events.

Aerosol pH was primarily influenced by the $\text{NH}_4^+/\text{NH}_3$ buffering pair, a result of excessive ammonia emissions in central China, maintaining medium acidity levels (Van Damme et al., 2018; Zheng et al., 2020). The mean and peak pH values followed the pattern WZ > BZ > ZZ, strongly

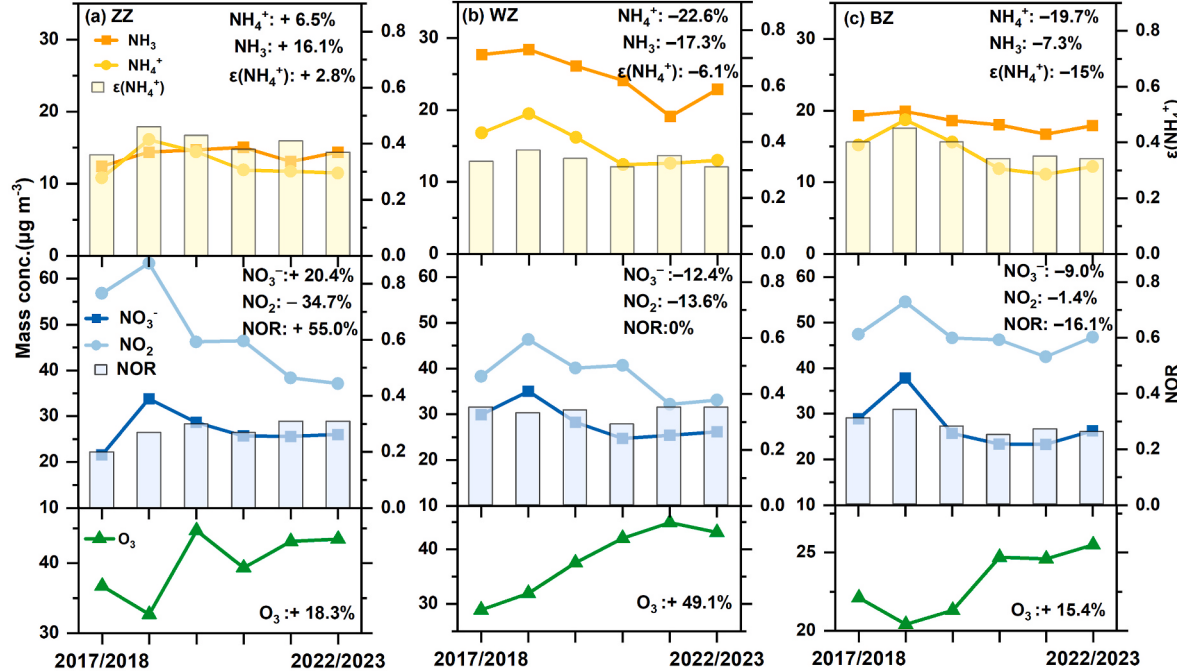


Fig. 3. Variation trends of NO_3^- , NO_2 , NOR, NH_4^+ , NH_3 , $\varepsilon(\text{NH}_4^+)$, and O_3 at (a) ZZ, (b) WZ, and (c) BZ sites in cold seasons from 2017/2018 to 2022/2023. NOR was defined as the molar ratio of $\text{NO}_3^- / (\text{NO}_3^- + \text{NO}_2)$. $\varepsilon(\text{NH}_4^+)$ was defined as the molar ratios of $\text{NH}_4^+ / (\text{NH}_4^+ + \text{NH}_3)$.

correlating with total NH_X concentrations and negatively with $\epsilon(\text{NH}_4^+)$. Minor inter-annual fluctuations were attributed to variations in temperature, humidity, and the ratio of TNNO_3 to TH_2SO_4 (Ding et al., 2019; Tao and Murphy, 2021). Hourly pH values across all three sites ranged from 4 to 6 (Fig. 4), consistent with trends observed in Tianjin and Beijing (Gao et al., 2020; Song et al., 2018). Notably, nitrate predominantly exists in particulate form ($\epsilon(\text{NO}_3^-) \approx 1$) when pH exceeded 3 during winter (Xu et al., 2024). Over 90 % of the sampling periods exhibited pH > 3 in our study, confirming the dominance of particulate nitrate in pollution events. At the WZ and ZZ sites, pH exhibited minimal inter-annual variability, while the BZ site experienced a decrease in mean pH from 5.71 in 2017/2018 to 4.95 in 2021/2022, accompanied

by an increase in $\epsilon(\text{NO}_3^-)$ from 0.83 to 0.97 (Tables S1, S2, and S3), suggesting enhanced conversion of gaseous nitric acid to particulate nitrate. Despite minimal increases in nitrate concentrations at WZ and BZ during the last three cold seasons, the enhanced conversion efficiency of gaseous nitric acid to particulate nitrate may hinder future abatement efforts.

The relationships between $\epsilon(\text{NH}_4^+)$, NO_3^- , and related chemical properties are shown in Fig. 4. Under medium acidity (pH = 3–7), NO_3^- concentrations increased with $\epsilon(\text{NH}_4^+)$, accompanied by decreasing pH and increasing AWC, consistent with findings from Guo et al.'s (2018) simulation study. The ZZ site was unique in that $\epsilon(\text{NH}_4^+)$ did not decrease, suggesting that the lack of response to NO_2 reduction at ZZ in

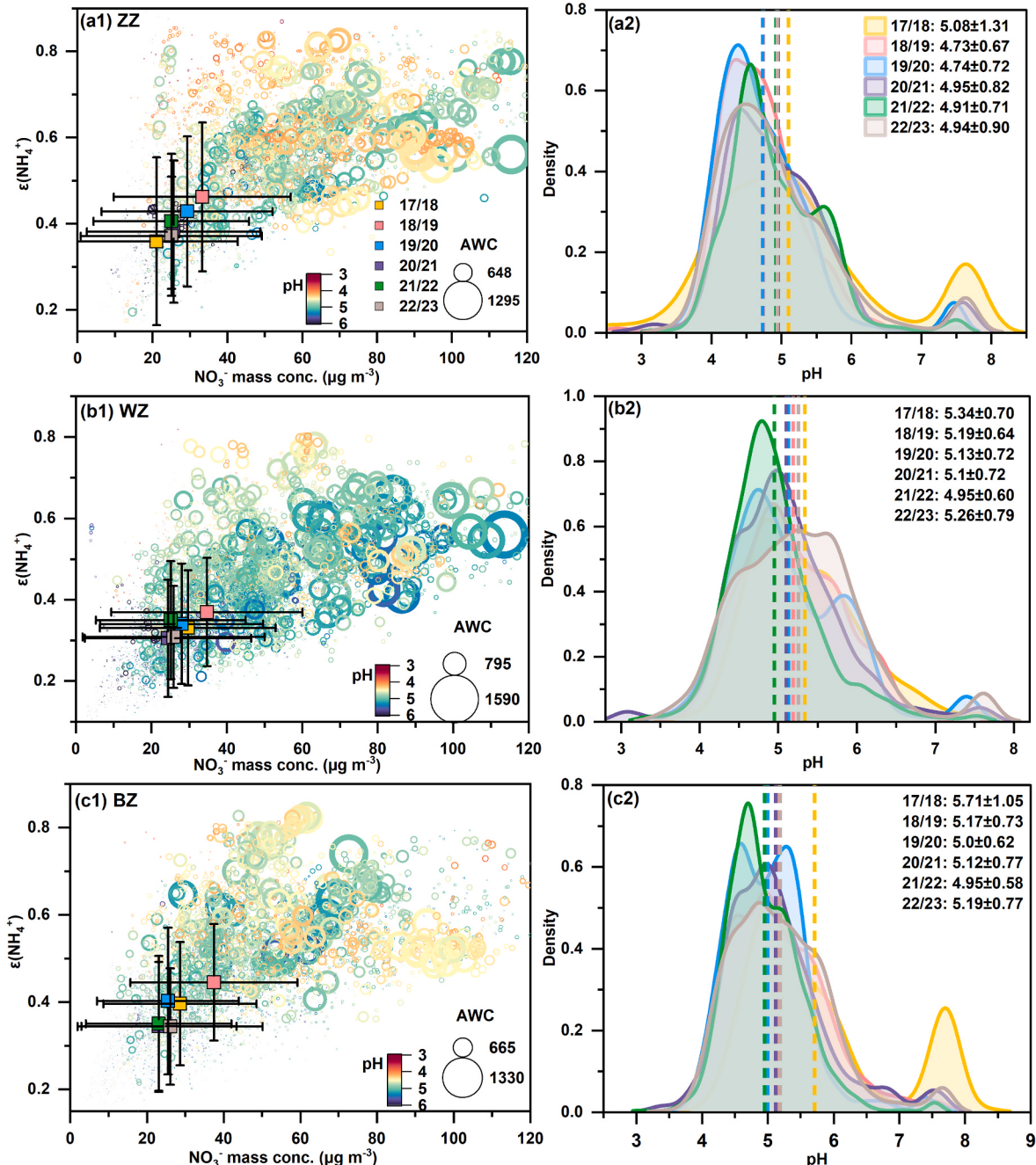


Fig. 4. The error bar charts and scatter plots between NO_3^- concentration and $\epsilon(\text{NH}_4^+)$ at (a1) ZZ, (b1) WZ, and (c1) BZ sites from 2017/2018 to 2022/2023, markers in error bar chart were colored according to different seasons, the diameter of the circles was scaled with the AWC value and the color represents the aerosol pH. The density plots of aerosol pH at (a2) ZZ, (b2) WZ, and (c2) BZ sites during cold seasons from 2017/2018 to 2022/2023. $\epsilon(\text{NH}_4^+)$ was defined as the molar ratios of $\text{NH}_4^+ / (\text{NH}_4^+ + \text{NH}_3)$.

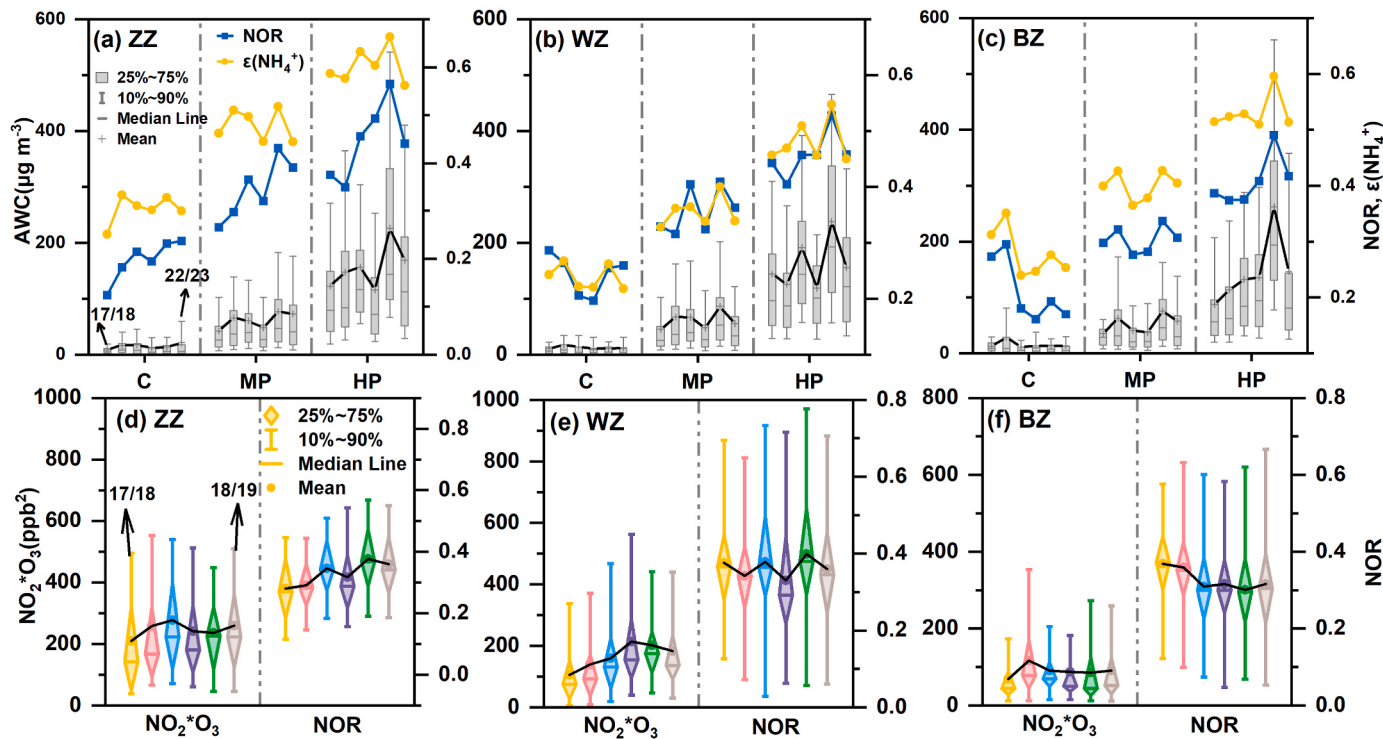


Fig. 5. The trends of AWC concentration, NOR, and $\epsilon(\text{NH}_4^+)$ under different $\text{PM}_{2.5}$ levels at (a) ZZ, (b) WZ, and (c) BZ sites in cold seasons from 2017/2018 to 2022/2023. The trends of NO_2^*O_3 , and NOR under nocturnal humidity $>50\%$ at (d) ZZ, (e) WZ, and (f) BZ sites in cold seasons from 2017/2018 to 2022/2023.

the past six winters could be explained by the slow synchronization of NH_3 and $\epsilon(\text{NH}_4^+)$ with NO_2 reductions, leading to higher particulate NO_3^- formation. At ZZ, the cold season NO_3^- concentration was significantly correlated with pH and AWC ($p \leq 0.05$, Fig. S7), suggesting that these factors, rather than precursors, primarily controlled NO_3^- levels. Similar findings have been observed in the U.S., where NH_3 and NO_3^- can remain in the gas phase during winter pollution episodes when $\text{pH} \leq 3$, though this requires extremely low ammonia concentrations, which is challenging in agricultural regions like central China (Guo et al., 2018; Jiang et al., 2022; Nah et al., 2018). During the last two cold seasons, NH_3 and NO_3^- levels at the BZ and WZ stations have not shown a sustained decline. This underscores the risk of increased nitrate formation if coordinated reductions in NH_3 and NO_2 emissions are not implemented in suburban and rural regions.

3.4. Effects of humidity and wind on nitrates

Given distinct diurnal meteorological conditions and nitrate formation pathways, we analyzed daytime and nighttime periods separately. As demonstrated by variations in nitrate mass concentrations and associated parameters across humidity gradients (Figs. 6 and 7; Section 3.5), particulate NO_3^- formation exhibits significant humidity dependence. In the first three cold seasons, substantial differences in NO_3^- concentrations were observed among the three sites, but these disparities diminished over time. Notably, under high humidity, the growth rate of NO_3^- was lower compared to drier conditions, a trend that mirrored changes in $\epsilon(\text{NH}_4^+)$. During the 2017/2018 season, the daytime growth rates at the BZ and WZ sites under $\text{RH} \leq 50\%$ were higher than those at ZZ (Fig. 6). However, by 2022/2023, all sites exhibited similar growth rates of approximately $1 \mu\text{g m}^{-3}$ per $1\% \text{RH}$. This increase was associated with a 30–50 % rise in O_3 concentrations, which served as the primary source of hydroxyl radicals (OH) in this humidity range. Above 50 % RH, NO_3^- growth plateaued, likely due to a reduction in photochemical reactions, with O_3 concentrations declining and nitrous acid (HONO) becoming a more significant OH source (Fu et al., 2019). At

higher RH (70–90 %), the highest concentrations of NO_3^- were observed, coinciding with peak aerosol acidity and $\epsilon(\text{NH}_4^+)$, signaling a sub-stable state of the aerosol. As RH approached saturation, photochemical reactions slowed, and NO_3^- transitioned into the liquid phase, halting further growth. The ZZ site exhibited the most significant increase in NOR, suggesting enhanced photochemical and heterogeneous reactions over the six years. The WZ site recorded the highest midday NOR (Figs. S9, S10, and S11), attributed to elevated O_3 and NH_3 concentrations (Fu et al., 2020).

At night, nitrate formation primarily occurs via the hydrolysis of N_2O_5 , which is absent of photochemical processes. Due to the absence of direct N_2O_5 measurements, nocturnal nitrate formation rate via N_2O_5 hydrolysis was estimated using the proxy $[\text{NO}_2] \times [\text{O}_3]$, following established methodologies by Zhou et al. (2022) and Yun et al. (2018). This approach leveraged the theoretical positive correlation between the proxy and the HNO_3 formation rate from N_2O_5 hydrolysis. Fig. 5 revealed an increasing annual trend in hydrolysis intensity across all three sites due to the nocturnal rising O_3 (Fig. 6), with ZZ exhibiting the highest values (about $200\text{--}300 \text{ ppb}^2[\text{NO}_2] \times [\text{O}_3]$) vs. WZ and BZ (about $100\text{--}200 \text{ ppb}^2$). Crucially, ZZ demonstrated a significant synergistic trend between nocturnal O_3 increases (Figs. 6 and 20 %–40 % elevation from 20:00 to 06:00 during 2022/2023 vs. 2017/2018) and elevated NH_3 levels (8 %–19 %), accelerating nitrate radical production via the $\text{NO}_2 + \text{O}_3 \rightarrow \text{NO}_3$ pathway and subsequently promoting N_2O_5 formation ($\text{NO}_2 + \text{NO}_3 \rightarrow \text{N}_2\text{O}_5$) and hydrolysis to NO_3^- , due to increased NOR at night (Fig. S11). Under moderate humidity (40–80 %), this process – synergized with high AWC – substantially enhanced hydrolysis efficiency, driving explosive NO_3^- growth, consistent with oxidation enhancement mechanisms as reported (Fig. 7, Zhang et al., 2024). Conversely, at WZ and BZ sites, nocturnal NH_3 decline (>15 %) effectively counteracted O_3 -driven oxidation enhancement, partially suppressing NOR growth. BZ exhibited stronger gas-phase nitrate formation under low humidity (RH < 50 %) due to transportation-related nocturnal NO_2 emissions, while WZ showed minimal NO_3^- growth during 2022/2023 low humidity periods, reflecting lower nocturnal NO_2

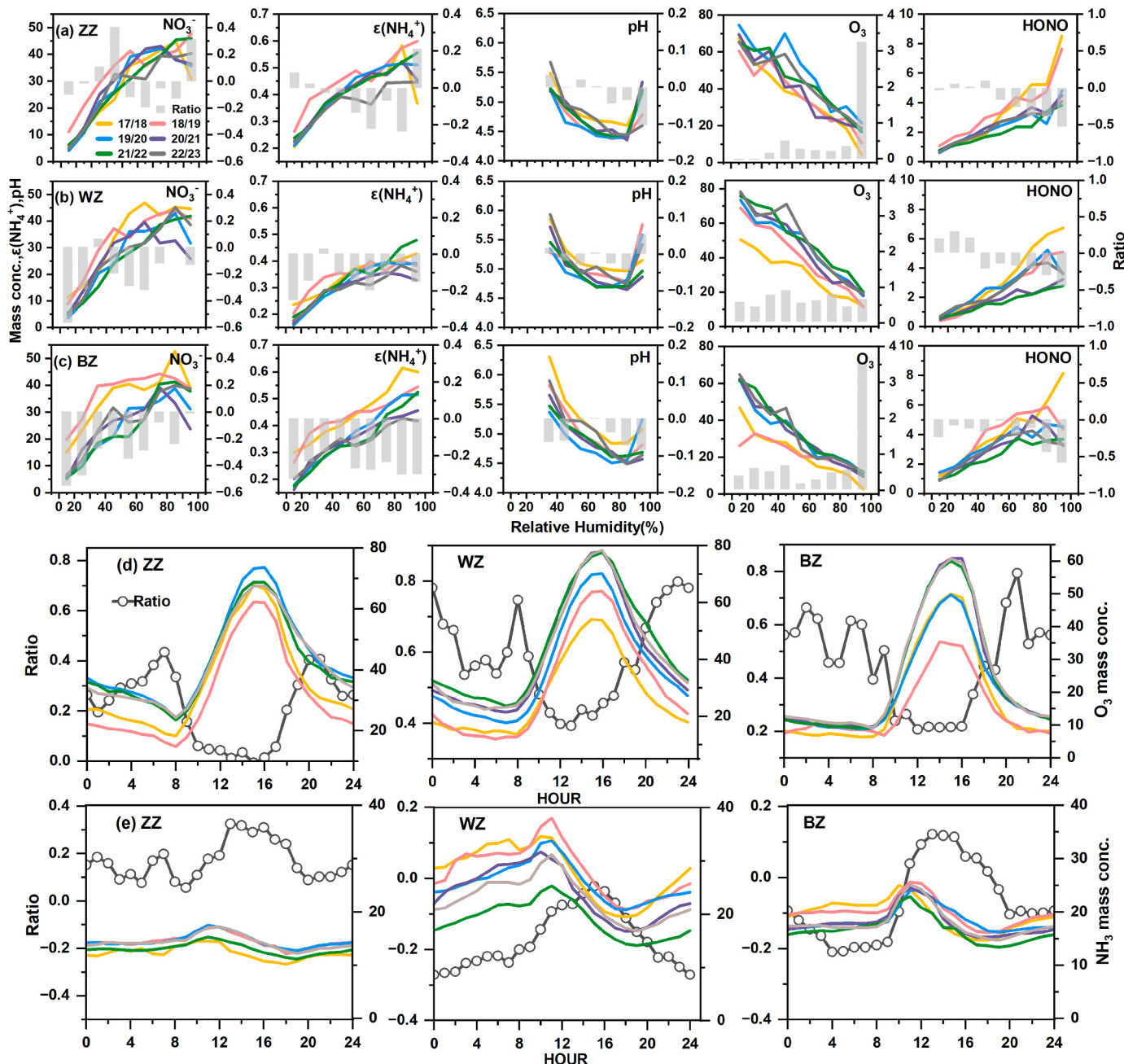


Fig. 6. Variations of NO_3^- , $\epsilon(\text{NH}_4^+)$, pH, O_3 , and HONO as a function of RH during daytime at (a) ZZ, (b) WZ, and (c) BZ sites in the cold seasons from 2017/2018 to 2022/2023. The gray dash bars indicate the ratio of the factor values for the specified humidity range during the 2022/2023 season compared to those during the 2017/2018 season. Diurnal variations of O_3 (d) and NH_3 (e) at ZZ, WZ, and BZ sites during cold seasons from 2017/2018 to 2022/2023. Dotted line plots demonstrate the ratio of O_3 and NH_3 during the 2022/2023 season compared to those during the 2017/2018 season at corresponding time points.

emissions. Near-saturation humidity universally reduced hydrolysis rates due to diminished O_3 concentrations and elevated aerosol pH. These patterns align with Wang et al. (2023), where urban NO_2 reductions were offset by O_3 and NH_3 variations. At WZ and BZ, stagnant NOR resulted from limited NO_2 reduction coupled with concurrent NH_3 decreases.

Wind direction also played a crucial role in the distribution of aerosol precursors. Polar plots revealed distinct source regions for NO_3^- and NH_4^+ concentrations at each site (Fig. S12). At ZZ, local generation dominated under stable atmospheric conditions, while at WZ, increased concentrations during southwest and northeast winds indicated significant regional transport of aged aerosols. The BZ site, with comparable source regions for NO_3^- , NH_4^+ , NO_2 , and NH_3 , reflected emissions from nearby

transportation hubs and industrial activities (Sheng et al., 2024). The potential source regions of annual pollution at each site varied minimally, indicating that regional coordinated control was crucial for mitigating aerosols.

3.5. Roles of Meteorology and emissions in nitrate trends

For NO_3^- simulations, the random forest model achieved R^2 values of 0.97–0.98 and RMSE of 2.8–5.2 (Table S5, Fig. S14–15), with both RMSE and residuals exhibiting normal distributions (Fig. S15–16), indicating acceptable performance closely with similar studies (W. Zhou et al., 2022; Zhang et al., 2020). The impacts of RH, wind direction, wind speed, temperature, pressure, and precipitation on the prediction

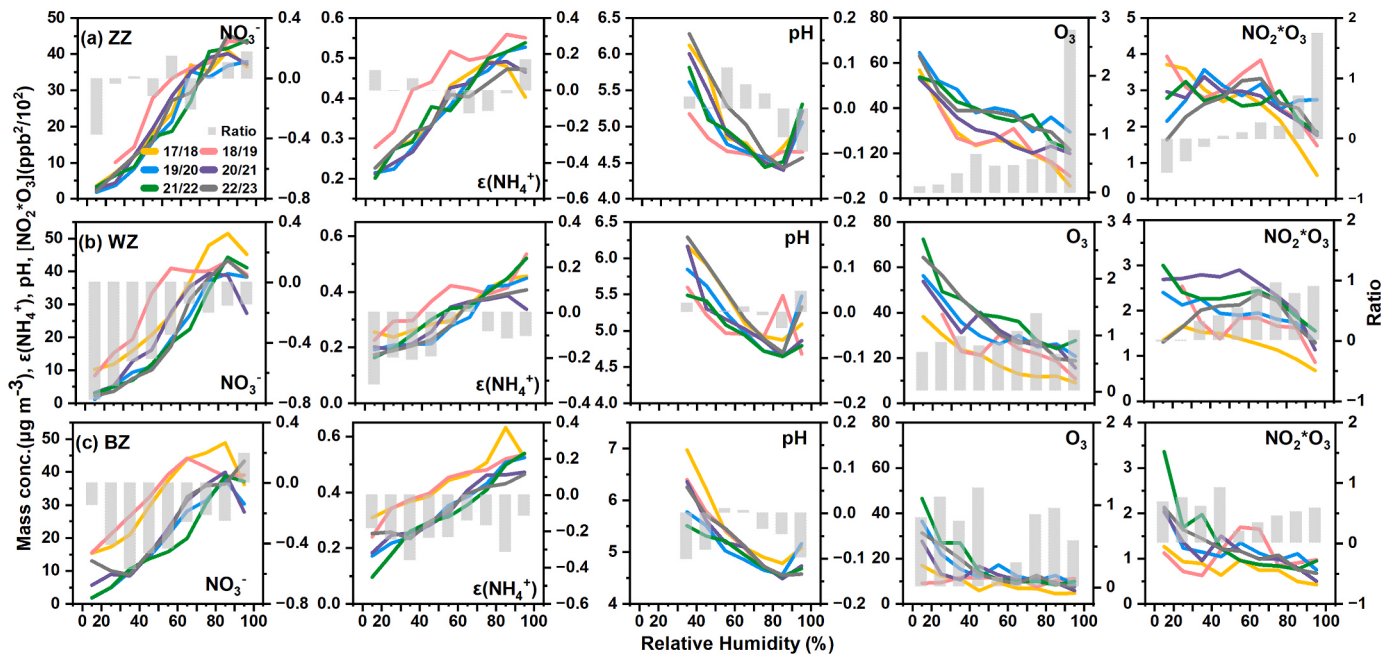


Fig. 7. Variations of NO_3^- , $\epsilon(\text{NH}_4^+)$, pH, O_3 , and $[\text{NO}_2]^*[\text{O}_3]$ as a function of RH during night at (a)ZZ, (b)WZ, and (c) BZ sites in the cold seasons from 2017/2018 to 2022/2023. The gray dash bars indicate the ratio of the factor values for the specified humidity range during the 2022/2023 season compared to those during the 2017/2018 season.

performance of NO_3^- were shown in Fig. 8, which revealed that RH dominated NO_3^- pollution variation across all three sites, followed by temperature and atmospheric pressure. The meteorologically normalized concentrations at the three monitoring sites were presented in Table S5 and Fig. 8. The long-term variations in de-weathered NO_3^- are

consistent with the observed data trends, suggesting that the changes in concentration trends at the three sites were primarily driven by variations in emission sources. Meteorological factors also played a significant role. After removing meteorological influences, the de-weathered nitrate concentration at the ZZ site increased from the observed 21.6 μg

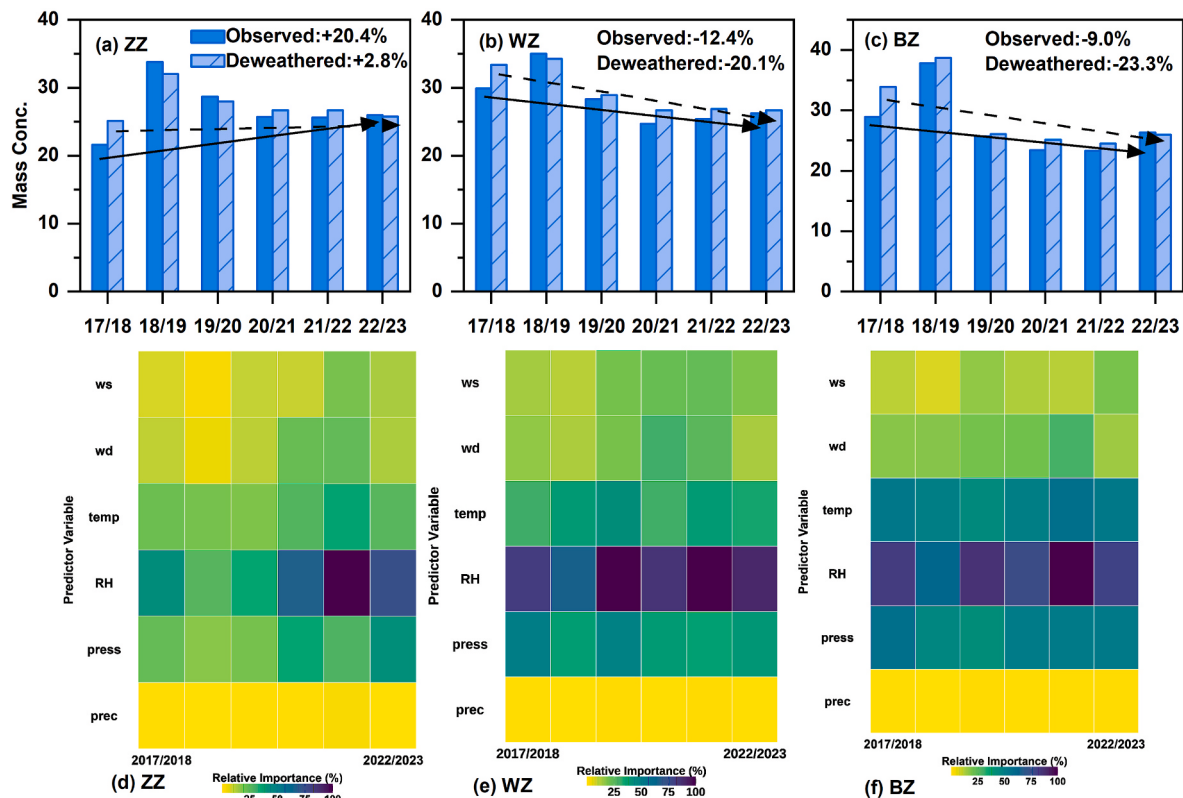


Fig. 8. Variations of observed NO_3^- and de-weathered NO_3^- concentrations at (a)ZZ, (b)WZ, and (c) BZ in cold seasons from 2017/2018 to 2022/2023. Importance of meteorological variables in the random forest model at (d)ZZ, (e)WZ, and (f) BZ in each season.

m^{-3} to $25.1 \mu g m^{-3}$ during the 2017/2018 cold season, indicating favorable meteorological conditions that period. In contrast, the 2022/2023 cold season showed minimal meteorological impact, with concentrations decreasing only slightly from observed $26 \mu g m^{-3}$ to $25.8 \mu g m^{-3}$. Over the six cold seasons, the de-weathered concentration increased by just 2.8%—significantly lower than the observed 20.4% growth. This demonstrated that emission changes alone still drove nitrate increases during this period, while meteorological conditions amplified this trend. For the WZ and BZ sites, de-weathered nitrate concentrations decreased by 20.1% and 23.3% respectively over the same period, exceeding the observed reductions. This indicated that emission changes at these sites effectively reduced nitrate levels; however, unfavorable meteorological conditions weakened the air quality improvement.

Therefore, both observational and modeling results indicate that at the urban ZZ site, uncoordinated NH_3 increases (+16.1%) and enhanced O_3 (+18.1%) weakened the response of NO_3^- to NO_2 reductions (-34.7%). This situation is similar to trends observed in other urban areas in China and the United States (Fu et al., 2017; Li et al., 2021; Shah et al., 2018; Zhai et al., 2021). In contrast, at rural WZ and suburban BZ, synchronized NH_3 – NO_2 co-reductions drove NO_3^- declines. However, meteorological changes partially offset these improvements. Notably, de-weathered NO_3^- showed no significant decrease since the 2020 COVID-19 pandemic, suggesting no further reductions in anthropogenic emissions over the past three cold seasons. Notably, January consistently exhibited the highest emission-driven nitrate levels across all sites (Fig. S13), underscoring the need for stricter controls during peak pollution months. These findings highlight the limited efficacy of urban NO_x -only policies and the critical role of NH_3 –oxidant co-management in rural and suburban regions.

4. Conclusion and Policy implications

This study elucidates the spatiotemporal variations in nitrate levels and their driving mechanisms in Central China. As a predominant component, the abatement effectiveness of nitrate will determine whether future $PM_{2.5}$ concentrations can sustain continuous improvement. In urban areas, the increase in NO_3^- , despite a reduction in NO_2 levels, is attributed to chemical feedback from uncoordinated NH_3 reductions and enhanced atmospheric oxidation. Conversely, suburban and rural sites saw simultaneous reductions in both NO_3^- and NO_2 , likely due to moderate decreases in agricultural NH_3 emissions. Model results further corroborate that, after removing meteorological influences, nitrate concentrations at the ZZ site still increased due to insufficient reductions in emissions, while precursor reductions contributed to nitrate decreases at WZ and BZ sites.

The study also identifies distinct nitrate formation pathways across urbanization gradients driven by localized chemical regimes. Urban areas predominantly exhibit enhanced heterogeneous N_2O_5 hydrolysis during nighttime, facilitated by reduced aerosol acidity and elevated AWC, while suburban sites showed stronger homogeneous reactions through NO_2 oxidation due to persistent NO_x emissions. Rural regions demonstrate unexpectedly nitrate conversion efficient despite lower precursor levels, attributed to optimal pH conditions and intensified ozone-mediated oxidation. Analysis of trends observed in rural and suburban areas over the last three cold seasons suggests a growing risk of nitrate rebound, driven by rising ozone levels and ammonia-mediated chemical feedback mechanisms.

The observed chemical feedback mechanisms, particularly ammonia-rich aerosol neutralization and oxidant-driven precursor conversion, highlight the inadequacy of conventional single-pollutant NO_x controls. This chemical regime necessitates coordinated NH_3 – NO_x mitigation strategies, particularly considering the dual advantages of NH_3 abatement: a 90% lower implementation cost compared to conventional controls and enhanced chemical leverage in particulate matter regulation (Gu et al., 2021, 2023; Guo et al., 2024).

Global precedents, such as SO_2 – NO_x –VOCs co-reduction under low NH_3 conditions in U.S. (Bin et al., 2024; Shah et al., 2018), reinforce the necessity of multi-pollutant strategies to sustain $PM_{2.5}$ improvements. In Central China's agricultural-industrial transition zones, unmitigated NH_3 emissions elevate aerosol pH and nitrate partitioning efficiency, perpetuating pollution persistence (Zheng et al., 2024). To address this, we propose an integrated framework: rural areas should prioritize agricultural NH_3 reduction through precision fertilization and livestock management to mitigate health risks and socioeconomic costs (Wyer et al., 2022); urban hotspots require targeted controls on non-agricultural NH_3 (e.g., industrial/vehicular sources) and oxidant precursors (e.g., VOCs); while transitional suburbs could adopt emission trading systems coupled with real-time aerosol monitoring to balance agricultural and industrial emissions (Liu et al., 2023; Yan et al., 2022). This strategy supports deep NO_x cuts in Chinese megacities and offers a scalable model to harmonize agricultural-industrial emissions in global urbanizing regions via multi-pollutant governance.

CRediT authorship contribution statement

Shuangliang Ma: Writing – original draft, Visualization, Validation, Data curation, Conceptualization. **Nan Wang:** Visualization, Software, Formal analysis, Conceptualization. **Jiani Zhang:** Formal analysis, Conceptualization. **Daiqi Ye:** Writing – review & editing, Supervision. **Lingling Wang:** Supervision, Project administration, Funding acquisition.

Declaration of competing interest

The authors declare that they have no known competing financial interests or personal relationships that could have appeared to influence the work reported in this paper.

Acknowledgements

This work was supported by the National Key Research and Development Program of China (Grant no. 2017YFC0212405, 2024YFC3713701, and 2024YFC3713702) and the Key Research and Development Program of Henan Province (Grant no. 201400210700).

Appendix A. Supplementary data

Supplementary data to this article can be found online at <https://doi.org/10.1016/j.jenvman.2025.126594>.

Data availability

I have shared the link to my data/code at the Attach File step

References

- Behera, S.N., 2011. Degradation of SO_2 , NO_2 and NH_3 leading to formation of secondary inorganic aerosols: an environmental chamber study. *Atmos. Environ.* 45, 4015–4024. <https://doi.org/10.1016/j.atmosenv.2011.04.056>.
- Bin, C., Kiran, A., Saravanan, A., 2024. Spatiotemporal trends in $PM_{2.5}$ chemical composition in the conterminous U.S. during 2006–2020. *Atmos. Environ.* 316, 120188. <https://doi.org/10.1016/j.atmosenv.2023.120188>.
- Brown, S.S., Dibb, J.E., Stark, H., Aldener, M., Vozella, M., Whitlow, S., Williams, E.J., Lerner, B.M., Jakoubek, R., Middlebrook, A.M., DeGouw, J.A., Warneke, C., Goldan, P.D., Kuster, W.C., Angevine, W.M., Sueper, D.T., Quinn, P.K., Bates, T.S., Meagher, J.F., Fehsenfeld, F.C., Ravishankara, A.R., 2004. Nighttime removal of NO_x in the summer marine boundary layer. *Geophys. Res. Lett.* 31, L07108. <https://doi.org/10.1029/2004GL019412>.
- Chen, X., Wang, H., Lu, K., Li, C., Zhai, T., Tan, Z., Ma, X., Yang, X., Liu, Y., Chen, S., Dong, H., Li, X., Wu, Z., Hu, M., Zeng, L., Zhang, Y., 2020. Field determination of nitrate Formation pathway in Winter Beijing. *Environ. Sci. Technol.* 54, 9243–9253. <https://doi.org/10.1021/acs.est.0c00972>.
- Cheng, Y., Zheng, G., Wei, C., Mu, Q., Zheng, B., Wang, Z., Gao, M., Zhang, Q., He, K., Carmichael, G., Pöschl, U., Su, H., 2016. Reactive nitrogen chemistry in aerosol

- water as a source of sulfate during haze events in China. *Sci. Adv.* 2, e1601530. <https://doi.org/10.1126/sciadv.1601530>.
- Ding, J., Zhao, P., Su, J., Dong, Q., Du, X., Zhang, Y., 2019. Aerosol pH and its driving factors in Beijing. *Atmos. Chem. Phys.* 19, 7939–7954. <https://doi.org/10.5194/acp-19-7939-2019>.
- Du, H., Li, J., Wang, Z., Dao, X., Guo, S., Wang, L., Ma, S., Wu, J., Yang, W., Chen, X., Sun, Y., 2020. Effects of regional transport on haze in the North China plain: transport of precursors or secondary inorganic aerosols. *Geophys. Res. Lett.* 47, e2020GL087461. <https://doi.org/10.1029/2020GL087461>.
- Feng, S., Wang, M., Heal, M.R., Liu, Xuejun, Liu, Xueyan, Zhao, Y., Strokal, M., Kroeez, C., Zhang, F., Xu, W., 2024. The impact of emissions controls on atmospheric nitrogen inputs to Chinese river basins highlights the urgency of ammonia abatement. *Sci. Adv.* 10, eadp2558. <https://doi.org/10.1126/sciadv.adp2558>.
- Fountoukis, C., Nenes, A., 2007. Isorropia II: a computationally efficient thermodynamic equilibrium model $K^+ \cdot Ca^{2+} \cdot Mg^{2+} \cdot NH_4^+ \cdot Na^+ \cdot SO_4^{2-} \cdot NO_3^- \cdot Cl^- \cdot H_2O$ aerosols. *Atmos. Chem. Phys.* 7, 4639–4659. <https://doi.org/10.5194/acp-7-4639-2007>.
- Fu, X., Wang, S., Xing, J., Zhang, X., Wang, T., Hao, J., 2017. Increasing Ammonia concentrations reduce the effectiveness of particle pollution control achieved via SO_2 and NO_x emissions reduction in East China. *Environ. Sci. Technol. Lett.* 4, 221–227. <https://doi.org/10.1021/acs.estlett.7b00143>.
- Fu, X., Wang, T., Gao, J., Wang, P., Liu, Y., Wang, S., Zhao, B., Xue, L., 2020. Persistent heavy winter nitrate pollution driven by increased photochemical oxidants in northern China. *Environ. Sci. Technol.* 54, 3881–3889. <https://doi.org/10.1021/acs.est.9b07248>.
- Fu, X., Wang, T., Zhang, L., Li, Q., Wang, Z., Xia, M., Yun, H., Wang, W., Yu, C., Yue, D., Zhou, Y., Zheng, J., Han, R., 2019. The significant contribution of HONO to secondary pollutants during a severe winter pollution event in southern China. *Atmos. Chem. Phys.* 19, 1–14. <https://doi.org/10.5194/acp-19-1-2019>.
- Gao, J., Wei, Y., Shi, G., Yu, H., Zhang, Z., Song, S., Wang, W., Liang, D., Feng, Y., 2020. Roles of RH, aerosol pH and sources in concentrations of secondary inorganic aerosols, during different pollution periods. *Atmos. Environ.* 241, 117770. <https://doi.org/10.1016/j.atmosenv.2020.117770>.
- Geng, G., Liu, Yuxi, Liu, Yang, Liu, S., Cheng, J., Yan, L., Wu, N., Hu, H., Tong, D., Zheng, B., Yin, Z., He, K., Zhang, Q., 2024. Efficacy of China's clean air actions to tackle $PM_{2.5}$ pollution between 2013 and 2020. *Nat. Geosci.* 17, 987–994. <https://doi.org/10.1038/s41561-024-01540-z>.
- Grange, S.K., Carslaw, D.C., Lewis, A.C., Boleti, E., Hueglin, C., 2018. Random forest meteorological normalisation models for Swiss PM_{10} trend analysis. *Atmos. Chem. Phys.* 18, 6223–6239. <https://doi.org/10.5194/acp-18-6223-2018>.
- Gu, B., Zhang, L., Van Dingenen, R., Vieno, M., Van Grinsven, H.J., Zhang, X., Zhang, S., Chen, Y., Wang, S., Ren, C., Rao, S., Holland, M., Winiwarter, W., Chen, D., Xu, J., Sutton, M.A., Chen, D., 2021. Abating ammonia is more cost-effective than nitrogen oxides for mitigating $PM_{2.5}$ air pollution. *Science* 374, 758–762. <https://doi.org/10.1126/science.abf8623>.
- Gu, B., Zhang, X., Lam, S.K., Yu, Y., Van Grinsven, H.J.M., Zhang, S., Wang, X., Bodirsky, B.L., Wang, S., Duan, J., Ren, C., Bouwman, L., De Vries, W., Xu, J., Sutton, M.A., Chen, D., 2023. Cost-effective mitigation of nitrogen pollution from global croplands. *Nature* 613, 77–84. <https://doi.org/10.1038/s41586-022-05481-8>.
- Guo, H., Otjes, R., Schlag, P., Kiendler-Scharr, A., Nenes, A., Weber, R.J., 2018. Effectiveness of ammonia reduction on control of fine particle nitrate. *Atmos. Chem. Phys.* 18, 12241–12256. <https://doi.org/10.5194/acp-18-12241-2018>.
- Guo, H., Xu, L., Bougiatioti, A., Cerully, K.M., Capps, S.L., Hite, J.R., Carlton, A.G., Lee, S.-H., Bergin, M.H., Ng, N.L., Nenes, A., Weber, R.J., 2015. Fine-particle water and pH in the southeastern United States. *Atmos. Chem. Phys.* 15, 5211–5228. <https://doi.org/10.5194/acp-15-5211-2015>.
- Guo, Y., Zhang, L., Winiwarter, W., Van Grinsven, H.J.M., Wang, X., Li, K., Pan, D., Liu, Z., Gu, B., 2024. Ambitious nitrogen abatement is required to mitigate future global $PM_{2.5}$ air pollution toward the world health organization targets. *One Earth* 7, 1600–1613. <https://doi.org/10.1016/j.oneear.2024.08.007>.
- Jiang, N., Wei, Y., Zhang, R., Hao, Q., Hao, X., Zhang, C., Hu, R., 2022. Modeling of reducing NH_4NO_3 in $PM_{2.5}$ under high ammonia emission in urban areas: based on high-resolution data. *J. Clean. Prod.* 350, 131499. <https://doi.org/10.1016/j.jclepro.2022.131499>.
- Lei, L., Zhou, W., Chen, C., He, Y., Li, Z., Sun, J., Tang, X., Fu, P., Wang, Z., Sun, Y., 2021. Long-term characterization of aerosol chemistry in cold season from 2013 to 2020 in Beijing, China. *Environ. Pollut.* 268, 115952. <https://doi.org/10.1016/j.envpol.2020.115952>.
- Li, X., Bei, N., Hu, B., Wu, J., Pan, Y., Wen, T., Liu, Z., Liu, L., Wang, R., Li, G., 2021. Mitigating NO_x emissions does not help alleviate wintertime particulate pollution in Beijing-Tianjin-Hebei, China. *Environ. Pollut.* 279, 116931. <https://doi.org/10.1016/j.envpol.2021.116931>.
- Liu, P., Li, X., Zhang, C., Mu, Y., 2023. It is time to reduce atmospheric pollutant emissions from agricultural and residential activities in rural China for the sustainable improvement of air quality. *Environ. Sci. Technol.* 57, 19102–19105. <https://doi.org/10.1021/acs.est.3c08670>.
- Liu, S., Geng, G., Xiao, Q., Zheng, Y., Liu, X., Cheng, J., Zhang, Q., 2022. Tracking daily concentrations of $PM_{2.5}$ Chemical composition in China since 2000. *Environ. Sci. Technol.* 56, 16517–16527. <https://doi.org/10.1021/acs.est.2c06510>.
- Liu, X., Zhang, Y., Han, W., Tang, A., Shen, J., Cui, Z., Vitousek, P., Erisman, J.W., Goulding, K., Christie, P., Fangmeier, A., Zhang, F., 2013. Enhanced nitrogen deposition over China. *Nature* 494, 459–462. <https://doi.org/10.1038/nature11917>.
- Nah, T., Guo, H., Sullivan, A.P., Chen, Y., Tanner, D.J., Nenes, A., Russell, A., Ng, N.L., Huey, L.G., Weber, R.J., 2018. Characterization of aerosol composition, aerosol acidity, and organic acid partitioning at an agriculturally intensive rural southeastern US site. *Atmos. Chem. Phys.* 18, 11471–11491. <https://doi.org/10.5194/acp-18-11471-2018>.
- Nie, D., Shen, F., Wang, J., Ma, X., Li, Z., Ge, P., Ou, Y., Jiang, Y., Chen, M., Chen, M., Wang, T., Ge, X., 2021. Changes of air quality and its associated health and economic burden in 31 provincial capital cities in China during COVID-19 pandemic. *Atmos. Res.* 249, 105328. <https://doi.org/10.1016/j.atmosres.2020.105328>.
- Pan, Y., Tian, S., Zhao, Y., Zhang, L., Zhu, X., Gao, J., Huang, W., Zhou, Y., Song, Y., Zhang, Q., Wang, Y., 2018. Identifying Ammonia hotspots in China using a national observation network. *Environ. Sci. Technol.* 52, 3926–3934. <https://doi.org/10.1021/acs.est.7b05235>.
- Qi, S., Zhao, S., Yu, Y., Yang, L., 2024. Composition, sources and potential source regions of aerosols under contrasting environment conditions of Lanzhou, a valley city of western China: observations by means of topographic relief. *Atmos. Pollut. Res.* 15, 102154. <https://doi.org/10.1016/j.apr.2024.102154>.
- Qu, Q., Wang, S., Zhao, B., Hu, R., Liang, C., Zhang, H., Li, S., Feng, B., Hou, X., Yin, D., Du, J., Chu, Y., Zhang, Y., Wu, Q., Wen, Y., Wu, X., Hu, J., Zhang, S., Hao, J., 2024. Response of organic aerosol in Beijing to emission reductions during the XXIV Olympic Winter Games. *Sci. Total Environ.* 914, 170033. <https://doi.org/10.1016/j.scitotenv.2024.170033>.
- Ryoo, I., Ren, L., Li, G., Zhou, T., Wang, M., Yang, X., Kim, T., Cheong, Y., Kim, S., Chae, H., Lee, K., Jeon, K., Hopke, P.K., Yi, S.-M., Park, J., 2024. Effects of seasonal management programs on $PM_{2.5}$ in Seoul and Beijing using DN-PMF: collaborative efforts from the Korea-China joint research. *Environ. Int.* 191, 108970. <https://doi.org/10.1016/j.envint.2024.108970>.
- Shah, V., Jaegle, L., Thornton, J.A., Lopez-Hilfiker, F.D., Lee, B.H., Schroder, J.C., Campuzano-Jost, P., Jimenez, J.L., Guo, H., Sullivan, A.P., Weber, R.J., Green, J.R., Fiddler, M.N., Billilign, S., Campos, T.L., Stell, M., Weinheimer, A.J., Montzka, D.D., Brown, S.S., 2018. Chemical feedbacks weaken the wintertime response of particulate sulfate and nitrate to emissions reductions over the eastern United States. *Proc. Natl. Acad. Sci. USA* 115, 8110–8115. <https://doi.org/10.1073/pnas.1803295115>.
- Sheng, H., Fan, L., Chen, M., Wang, H., Huang, H., Ye, D., 2024. Identification of NO_x emissions and source characteristics by TROPOMI observations – a case study in north-central Henan, China. *Sci. Total Environ.* 931, 172779. <https://doi.org/10.1016/j.scitotenv.2024.172779>.
- Shi, Z., Song, C., Liu, B., Lu, G., Xu, J., Van Vu, T., Elliott, R.J.R., Li, W., Bloss, W.J., Harrison, R.M., 2021. Abrupt but smaller than expected changes in surface air quality attributable to COVID-19 lockdowns. *Sci. Adv.* 7, eabd6696. <https://doi.org/10.1126/sciadv.abd6696>.
- Song, S., Gao, M., Xu, W., Shao, J., Shi, G., Wang, S., Wang, Y., Sun, Y., McElroy, M.B., 2018. Fine-particle pH for Beijing winter haze as inferred from different thermodynamic equilibrium models. *Atmos. Chem. Phys.* 18, 7423–7438. <https://doi.org/10.5194/acp-18-7423-2018>.
- Sun, Y., Lei, L., Zhou, W., Chen, C., He, Y., Sun, J., Li, Z., Xu, W., Wang, Q., Ji, D., Fu, P., Wang, Z., Worsnop, D.R., 2020. A chemical cocktail during the COVID-19 outbreak in Beijing, China: insights from six-year aerosol particle composition measurements during the Chinese New Year holiday. *Sci. Total Environ.* 742, 140739. <https://doi.org/10.1016/j.scitotenv.2020.140739>.
- Tao, Y., Murphy, J.G., 2021. Simple framework to quantify the contributions from different factors influencing aerosol pH based on NH_3 phase-partitioning equilibrium. *Environ. Sci. Technol.* 55, 10310–10319. <https://doi.org/10.1021/acs.est.1c03103>.
- Tian, Y., Ma, Y., Wu, J., Wu, Y., Wu, T., Hu, Y., Wei, J., 2024. Ambient $PM_{2.5}$ chemical composition and cardiovascular disease hospitalizations in China. *Environ. Sci. Technol.* 58, 16327–16335. <https://doi.org/10.1016/j.est.4c05718>.
- Turpin, B.J., Lim, H.J., 2001. Species contributions to $PM_{2.5}$ mass concentrations: revisiting common assumptions for estimating organic mass. *Aerosol Sci. Technol.* 35, 602–610. <https://doi.org/10.1080/0278620119445>.
- Vu, T.V., Shi, Z., Cheng, J., Zhang, Q., He, K., Wang, S., Harrison, R.M., 2019. Assessing the impact of clean air action on air quality trends in Beijing using a machine learning technique. *Atmos. Chem. Phys.* 19, 11303–11314. <https://doi.org/10.5194/acp-19-11303-2019>.
- Van Damme, M., Clarisse, L., Whitham, S., Hadji-Lazaro, J., Hurtmans, D., Clerbaux, C., Coheur, P.-F., 2018. Industrial and agricultural ammonia point sources exposed. *Nature* 564, 99–103. <https://doi.org/10.1038/s41586-018-0747-1>.
- Wang, H., Wang, H.L., Lu, X., Lu, K., Zhang, L., Tham, Y.J., Shi, Z., Aikin, K., Fan, S., Brown, S.S., Zhang, Y., 2023. Increased night-time oxidation over China despite widespread decrease across the globe. *Nat. Geosci.* 16, 217–223. <https://doi.org/10.1038/s41561-022-01122-x>.
- Wang, H., Lu, K., Chen, X., Zhu, Q., Wu, Z., Wu, Y., Sun, K., 2018. Fast particulate nitrate formation via N_2O_5 uptake aloft in winter in Beijing. *Atmos. Chem. Phys.* 18, 10483–10495. <https://doi.org/10.5194/acp-18-10483-2018>.
- Wang, N., Zhou, L., Feng, M., Song, T., Zhao, Z., Song, D., Tan, Q., Yang, F., 2023. Progressively narrow the gap of $PM_{2.5}$ pollution characteristics at urban and suburban sites in a megacity of Sichuan Basin, China. *J. Environ. Sci.* 126, 708–721. <https://doi.org/10.1016/j.jes.2022.05.017>.
- Wang, S., Wang, L., Fan, X., Wang, N., Ma, S., Zhang, R., 2022. Formation pathway of secondary inorganic aerosols and its influencing factors in northern China: comparison between urban and rural sites. *Sci. Total Environ.* 840, 156404. <https://doi.org/10.1016/j.scitotenv.2022.156404>.
- Wyer, K.E., Kelleghan, D.B., Blanes-Vidal, V., Schauberger, G., Curran, T.P., 2022. Ammonia emissions from agriculture and their contribution to fine particulate matter: a review of implications for human health. *J. Environ. Manag.* 323, 116285. <https://doi.org/10.1016/j.jenvman.2022.116285>.
- Xu, B., Yu, H., Shi, Z., Liu, J., Wei, Y., Zhang, Z., Huangfu, Y., Xu, H., Li, Y., Zhang, L., Feng, Y., Shi, G., 2024. Knowledge-guided machine learning reveals pivotal drivers

- for gas-to-particle conversion of atmospheric nitrate. Environ. Sci. Ecotechnol. 19, 100333. <https://doi.org/10.1016/j.ese.2023.100333>.
- Yan, Y., Duan, X., Xie, K., Peng, L., Xu, Y., Niu, Y., Chen, H., 2022. Effectiveness of synergistic abatement for emissions of NO_x and NH₃ to mitigate nitrate-dominated aerosols in a typical city, northern China. Atmos. Environ. 289, 119325. <https://doi.org/10.1016/j.atmosenv.2022.119325>.
- Yang, W., Li, J., Wang, Z., Wang, L., Dao, X., Zhu, L., Pan, X., Li, Y., Sun, Y., Ma, S., Wang, W., Chen, X., Wu, J., 2021. Source apportionment of PM_{2.5} in the most polluted central plains economic Region in China: implications for joint prevention and control of atmospheric pollution. J. Clean. Prod. 283, 124557. <https://doi.org/10.1016/j.jclepro.2020.124557>.
- Yun, H., Wang, W., Wang, T., Xia, M., Yu, C., Wang, Z., Poon, S.C.N., Yue, D., Zhou, Y., 2018. Nitrate formation from heterogeneous uptake of dinitrogen pentoxide during a severe winter haze in southern China. Atmos. Chem. Phys. 18, 17515–17527. <https://doi.org/10.5194/acp-18-17515-2018>.
- Zhai, S., Jacob, D.J., Wang, X., Liu, Z., Wen, T., Shah, V., Li, K., Moch, J.M., Bates, K.H., Song, S., Shen, L., Zhang, Y., Luo, G., Yu, F., Sun, Y., Wang, L., Qi, M., Tao, J., Gui, K., Xu, H., Zhang, Q., Zhao, T., Wang, Y., Lee, H.C., Choi, H., Liao, H., 2021. Control of particulate nitrate air pollution in China. Nat. Geosci. 14, 389–395. <https://doi.org/10.1038/s41561-021-00726-z>.
- Zhang, Y., Vu, T.V., Sun, J., He, J., Shen, X., Lin, W., Zhang, X., Zhong, J., Gao, W., Wang, Y., Fu, T.M., Ma, Y., Li, W., Shi, Z., 2020. Significant changes in chemistry of fine particles in wintertime Beijing from 2007 to 2017: impact of clean air actions. Environ. Sci. Technol. 54, 1344–1352. <https://doi.org/10.1021/acs.est.9b04678>.
- Zhang, Z., Lu, B., Liu, C., Meng, X., Jiang, J., Herrmann, H., Chen, J., Li, X., 2024. Nitrate pollution deterioration in winter driven by surface ozone increase. npj Clim. Atmos. Sci. 7, 160. <https://doi.org/10.1038/s41612-024-00667-5>.
- Zheng, G., Su, H., Wang, S., Andreae, M.O., Pöschl, U., Cheng, Y., 2020. Multiphase buffer theory explains contrasts in atmospheric aerosol acidity. Science 369, 1374–1377. <https://doi.org/10.1126/science.aba3719>.
- Zheng, H., Kong, S., Zhai, S., Sun, X., Cheng, Y., Yao, L., Song, C., Zheng, Z., Shi, Z., Harrison, R.M., 2023. An intercomparison of weather normalization of PM_{2.5} concentration using traditional statistical methods, machine learning, and chemistry transport models. npj Clim. Atmos. Sci. 6, 214. <https://doi.org/10.1038/s41612-023-00536-7>, 2023.
- Zheng, M., Xu, C., Wan, Z., Cao, M., Xu, K., Chen, N., 2024. Reduction potential of ammonia emissions and impact on PM_{2.5} in a megacity of central China. Environ. Pollut. 343, 123172. <https://doi.org/10.1016/j.envpol.2023.123172>.
- Zhou, M., Nie, W., Qiao, L., Huang, D.D., Zhu, S., Lou, S., Wang, H., Wang, Q., Tao, S., Sun, P., Liu, Y., Xu, Z., An, J., Yan, R., Su, H., Huang, C., Ding, A., Chen, C., 2022a. Elevated formation of particulate nitrate from N₂O₅ hydrolysis in the Yangtze River Delta region from 2011 to 2019. Geophys. Res. Lett. 49, e2021GL097393. <https://doi.org/10.1029/2021GL097393>.
- Zhou, M., Zheng, G., Wang, H., Qiao, L., Zhu, S., Huang, D., An, J., Lou, S., Tao, S., Wang, Q., Yan, R., Ma, Y., Chen, C., Cheng, Y., Su, H., Huang, C., 2022b. Long-term trends and drivers of aerosol pH in eastern China. Atmos. Chem. Phys. 22, 13833–13844. <https://doi.org/10.5194/acp-22-13833-2022>.
- Zhou, W., Xu, W., Wang, Q., Li, Y., Lei, L., Yang, Y., Zhang, Z., Fu, P., Wang, Z., Sun, Y., 2022. Machine learning elucidates the impact of short-term emission changes on air pollution in Beijing. Atmos. Environ. 283, 119192. <https://doi.org/10.1016/j.atmosenv.2022.119192>.